

A Numerical Analysis of Supersonic Intake Buzz in an Axisymmetric Ramjet Engine

Hyo-Won Yeom*

Department of Aerospace and Mechanical Engineering, Korea Aerospace University, Goyang 412-791, Korea

Hong-Gye Sung**

School of Aerospace and Mechanical Engineering, Korea Aerospace University, Goyang 412-791, Korea

Vigor Yang***

School of Aerospace Engineering, Georgia Institute of Technology, Atlanta Georgia 30332, USA

Abstract

A numerical analysis was conducted to investigate the inlet buzz and combustion oscillation in an axisymmetric ramjet engine with wedge-type flame holders. The physical model of concern includes the entire engine flow path, extending from the leading edge of the inlet center-body through the exhaust nozzle. The theoretical formulation is based on the Favre-averaged conservation equations of mass, momentum, energy, and species concentration, and accommodates finite-rate chemical kinetics and variable thermo-physical properties. Turbulence closure is achieved using a combined scheme comprising of a low-Reynolds number $k-\varepsilon$ two-equation model and Sarkar's compressible turbulence model. Detailed flow phenomena such as inlet flow aerodynamics, flame evolution, and acoustic excitation as well as their interactions, are investigated. Mechanisms responsible for driving the inlet buzz are identified and quantified for the engine operating at subcritical conditions.

Key words: Ramjet Engine, Inlet Buzz, Combustion Oscillation, Compressible Turbulence Model

Nomenclature

A	= model constant of Arrhenius equation
a_1, a_3, a_5	= model constant of damping factor
C_k	= model constant of turbulent time scale
$C_{\varepsilon 1}, C_{\varepsilon 2}$	= model constants of turbulent energy dissipation
C_μ	= model constant of turbulent viscosity
c	= speed of sound
D	= diffusivity
E	= specific total energy
E_a	= activation energy
h	= specific enthalpy
k	= turbulent kinetic energy

k_f, k_{br}	= forward/backward reaction rate of r th reaction
L	= total length of domain of the grid dependency test
M_t	= turbulent Mach number
P	= static pressure
P_k	= production of kinetic energy
q_x, q_y	= heat flux
q_{xs}, q_{ys}	= diffusional flux of species s
R_u	= universal gas constant
b	= mass stoichiometric ratio
T	= static temperature
T_{turb}	= turbulent time scale
t	= time
u, v	= velocity
x, y	= spatial coordinate

This is an Open Access article distributed under the terms of the Creative Commons Attribution Non-Commercial License (<http://creativecommons.org/licenses/by-nc/3.0/>) which permits unrestricted non-commercial use, distribution, and reproduction in any medium, provided the original work is properly cited.

© * Currently Researcher, Defense Agency for Technology and Quality
** Professor, Corresponding author: hgsung@kau.ac.kr
*** William R.T. Professor

Y_s	= mass fraction of species s
W_s	= molecular weight of species s
$\alpha_1, \alpha_1, \alpha_1$	= model constants for compressible correction
β	= model constant for eddy dissipation concept
γ	= specific heat ratio
ε_c	= compressible dissipation
ε_s	= dissipation rate
A	= damping function
μ	= molecular viscosity
μ_t	= turbulent viscosity
ρ	= density
$\sigma_k, \sigma_\varepsilon$	= model constants
τ	= viscous stress tensor
τ_k	= Kolmogorov time scale
ν_{ir}', ν_{ir}''	= stoichiometric coefficients of species k of r th reaction

Subscripts

i, j	= spatial coordinate index
s	= species

Superscripts

$-$	= time average
\sim	= Favre average
$''$	= fluctuation associated with mass-weighted mean

1. Introduction

Supersonic ramjet engines typically operate at supercritical conditions to achieve reasonable system performance while maintaining a sufficient inlet shock stability margin. Undesired low-frequency inlet flow oscillations, a phenomena commonly referred to as buzz, may arise when the engine operates in the subcritical regime, and subsequently deteriorate the system stability and performance due to the ensuing flow oscillation, combustion instability, engine surge, thrust loss, etc. In the worst scenario, engine unstart occurs and causes the system failure.

Inlet buzz was first documented by Oswatitsch in 1947[1]. A series of studies was then conducted in the 1950s [2-6], primarily based on limited experimental measurements and linear stability analyses [2-6]. In the 1980s, motivated by the needs to circumvent ramjet combustion instability problems, Sajben and co-workers performed experimental studies on inlet diffuser flows with pressure oscillations [7-9]. Several related studies were also conducted to explore the internal flow-fields in ramjet engines, with special attention focused on the inlet aerodynamics [10-12] and combustion

chamber dynamics [13-14]. Newsome[15] and Lu and Jain [16] performed numerical simulations of subcritical inlet aerodynamic and the buzz phenomenon. More recently, Oh et al. [17] investigated the response of the flow-field in a supersonic inlet to acoustic oscillations arising from the downstream region.

Most of the above studies, except Ref. 13, treated either the inlet or the combustor individually. The physical characteristics involved in an entire engine have not been thoroughly understood. Hsieh and Yang [18] developed an integrated numerical framework for treating the flow and flame evolution in the entire flow path of an axisymmetric engine. Sung and Yang [19, 20] later examined the ignition transient process and the key mechanisms for driving and sustaining the inlet shock and combustion oscillations. Low-frequency longitudinal pressure oscillations were observed due to the interactions between the inlet and combustor flow dynamics. The purpose of the present work is to conduct a unified analysis of the flow-field in an entire ramjet engine. The physical model of concern extends from the leading edge of the inlet center-body to the exhaust nozzle, so that various unsteady flow and flame characteristics can be explored systematically. Special attention is given to the mutual coupling between the inlet buzz and combustion oscillation.

2. Numerical Method

The theoretical formulation is based on the Favre-averaged conservation equations in axisymmetric coordinates, and accommodates finite-rate chemical kinetics and variable thermo-physical properties. Turbulence closure is achieved using a combined model of the low-Reynolds-number κ - ε two-equation[23] and Sarkar's compressible-flow turbulent model[24-26]. The governing equations are solved numerically by means of a finite-volume, preconditioned flux-differencing scheme capable of treating a chemically reacting flow over a wide range of Mach numbers. The code is paralleled with a multi-block feature by using an MPI library to speed up the calculation.

2.1 Governing Equations

The Favre-averaged governing equations for the conservation of mass, momentum, energy, and species concentration for a chemically reacting flow can be written as:

$$\frac{\partial \mathbf{Q}}{\partial t} + \frac{\partial (\mathbf{E} - \mathbf{E}_v)}{\partial x} + \frac{\partial (\mathbf{F} - \mathbf{F}_v)}{\partial y} + \alpha \mathbf{H}_{\text{axi}} = \alpha \mathbf{H}_{\text{axi},v} + \mathbf{H} \quad (1)$$

$$\begin{aligned} \mathbf{Q} &= (\bar{\rho}, \bar{\rho}\bar{u}, \bar{\rho}\bar{v}, \bar{\rho}\bar{E}, \bar{\rho}\bar{k}, \bar{\rho}\bar{\varepsilon}, \bar{\rho}\bar{Y}_s)^T \\ \mathbf{E} &= (\bar{\rho}\bar{u}, \bar{\rho}\bar{u}^2 + \bar{p}, \bar{\rho}\bar{u}\bar{v}, (\bar{\rho}\bar{E} + \bar{p})\bar{u}, \bar{\rho}\bar{k}\bar{u}, \bar{\rho}\bar{\varepsilon}\bar{u}, \bar{\rho}\bar{u}\bar{Y}_s)^T \\ \mathbf{F} &= (\bar{\rho}\bar{v}, \bar{\rho}\bar{u}\bar{v}, \bar{\rho}\bar{v}^2 + \bar{p}, (\bar{\rho}\bar{E} + \bar{p})\bar{v}, \bar{\rho}\bar{k}\bar{v}, \bar{\rho}\bar{\varepsilon}\bar{v}, \bar{\rho}\bar{v}\bar{Y}_s)^T \end{aligned} \quad (2)$$

$$\begin{aligned} \mathbf{E}_v &= (0, \bar{\tau}_{xx}, \bar{\tau}_{xy}, \bar{u}\bar{\tau}_{xx} + \bar{v}\bar{\tau}_{xy} - \bar{q}_x, \bar{\tau}_{xx}, \bar{\tau}_{xy}, \bar{q}_{xs})^T \\ \mathbf{F}_v &= (0, \bar{\tau}_{yx}, \bar{\tau}_{yy}, \bar{u}\bar{\tau}_{yx} + \bar{v}\bar{\tau}_{yy} - \bar{q}_y, \bar{\tau}_{yx}, \bar{\tau}_{yy}, \bar{q}_{ys})^T \\ \mathbf{H}_{\text{axi}} &= \frac{1}{y} (\bar{\rho}\bar{v}, \bar{\rho}\bar{u}\bar{v}, \bar{\rho}\bar{v}^2, (\bar{\rho}\bar{E} + \bar{p})\bar{v}, \bar{\rho}\bar{k}\bar{v}, \bar{\rho}\bar{\varepsilon}\bar{v}, \bar{\rho}\bar{Y}_s\bar{v})^T \end{aligned} \quad (3)$$

$$\mathbf{H}_{\text{axi},v} = \frac{1}{y} \begin{pmatrix} 0 \\ \bar{\tau}_{xy} - \frac{2}{3}y \frac{\partial}{\partial x} \left(\mu_e \frac{\bar{v}}{y} \right) \\ \bar{\tau}_{yy} - \bar{\tau}_{\theta\theta} - \frac{2}{3} \frac{\mu_e \bar{v}}{y} - \frac{2}{3}y \frac{\partial}{\partial y} \left(\mu_e \frac{\bar{v}}{y} \right) \\ \bar{u}\bar{\tau}_{xy} + \bar{v}\bar{\tau}_{yy} - \bar{q}_y - \frac{2}{3} \frac{\mu_e \bar{v}^2}{y} - \frac{2}{3}y \frac{\partial}{\partial y} \left(\mu_e \frac{\bar{v}^2}{y} \right) - \frac{2}{3}y \frac{\partial}{\partial x} \left(\mu_e \frac{\bar{u}\bar{v}}{y} \right) \\ \bar{\tau}_{ky} \\ \bar{\tau}_{xy} \\ \bar{q}_{ys} \end{pmatrix} \quad (4)$$

$$\begin{aligned} \bar{\tau}_{xx} &= \mu_e \left(2 \frac{\partial \bar{u}}{\partial x} - \frac{2}{3} \left(\frac{\partial \bar{u}}{\partial x} + \frac{\partial \bar{v}}{\partial y} \right) \right), \quad \bar{\tau}_{yy} = \mu_e \left(2 \frac{\partial \bar{v}}{\partial y} - \frac{2}{3} \left(\frac{\partial \bar{u}}{\partial x} + \frac{\partial \bar{v}}{\partial y} \right) \right), \\ \bar{\tau}_{xy} &= \bar{\tau}_{yx} = \mu_e \left(\frac{\partial \bar{u}}{\partial x} + \frac{\partial \bar{v}}{\partial y} \right), \quad \bar{\tau}_{\theta\theta} = -\mu_e \left(\frac{2}{3} \left(\frac{\partial \bar{u}}{\partial x} + \frac{\partial \bar{v}}{\partial y} \right) + \frac{4}{3} \mu_e \frac{\partial \bar{v}}{\partial y} \right) \\ \bar{\tau}_{kx} &= \left(\mu + \frac{\mu_t}{\sigma_k} \right) \frac{\partial \bar{k}}{\partial x}, \quad \bar{\tau}_{ky} = \left(\mu + \frac{\mu_t}{\sigma_k} \right) \frac{\partial \bar{k}}{\partial y}, \quad \bar{\tau}_{\varepsilon x} = \left(\mu + \frac{\mu_t}{\sigma_\varepsilon} \right) \frac{\partial \bar{\varepsilon}}{\partial x}, \quad \bar{\tau}_{\varepsilon y} = \left(\mu + \frac{\mu_t}{\sigma_\varepsilon} \right) \frac{\partial \bar{\varepsilon}}{\partial y} \end{aligned} \quad (5)$$

The source vector \mathbf{H} includes source terms associated with gas injection, chemical reaction, and turbulence. For an axisymmetric calculation, α is 1.

For a multi-component mixture, specific total energy and specific internal energy can be written as follows;

$$E = e + \frac{u_i u_i}{2}, \quad e = h - \frac{p}{\rho} \quad (6)$$

$$h = \sum_{s=1}^N Y_s h_s = \sum_{s=1}^N Y_s \left(\Delta h_{f,s} + \int_{T_{ref}}^T C_{p,s}(T') dT' \right) \quad (7)$$

$$p = \rho R_u T \sum_{s=1}^N \frac{Y_s}{W_s} \quad (8)$$

where h_s and W_s are the specific enthalpy and molecular weight of species k , respectively, and R_u the universal gas constant. The pressure is evaluated from the ideal gas for a mixture of thermally perfect gas. A global reaction mechanism is applied to describe the chemical kinetics. In order to evaluate rate of a chemical reaction, Arrhenius equation and eddy dissipation model are implemented for the consideration of the turbulent combustion [21, 22]. β is model constant of 2.0.

$$\dot{\omega}_{\text{Arrhenius}} = W_s \sum_{r=1}^{N_k} \left(\nu_{sr} - \nu_{sr}' \right) \left(\left(k_{fr} \prod_{s=1}^N \left(\frac{\rho Y_s}{W_s} \right)^{\nu_{sr}'} \right)^{\nu_{sr}} - \left(k_{br} \prod_{s=1}^N \left(\frac{\rho Y_s}{W_s} \right)^{\nu_{sr}} \right)^{\nu_{sr}'} \right) \quad (9)$$

$$k = A \exp(-E_a / R_u T) [C_{12} H_{23}]^{0.25} [O_2]^{1.5} \quad (10)$$

$$A = 3.0 \times 10^{11} \text{ in cgs unit, } E_a = 30 \text{ kcal/mol}$$

$$\dot{\omega}_{\text{EDC}} = 4.0 \rho \frac{\varepsilon}{k} \text{Min} \left(Y_{\text{fuel}}, \frac{Y_{\text{oxy}}}{b}, \beta \frac{Y_{\text{prod}}}{(1+b)} \right) \quad (11)$$

$$\dot{\omega} = \text{Min}(\dot{\omega}_{\text{Arrhenius}}, \dot{\omega}_{\text{EDC}}) \quad (12)$$

2.2 Turbulence Closure

The standard k- ε model, which was proposed for high Reynolds number flows, is traditionally used with a wall function. Such an approach, however, encounters a singularity problem on the wall for flows with separation. Thus, a low Reynolds number k- ε model was developed for the near-wall turbulence. Within certain distances from the wall, all energetic large eddies reduce to Kolmogorov eddies, and all the important wall parameters such as friction velocity, viscous length scale, and mean strain rate at the wall can be characterized by the Kolmogorov micro scale. Yang and Shih [23] proposed a time-scale-based k- ε model for the near-wall turbulence using the Kolmogorov time scale as its lower bound. The equation can be integrated all the way to the wall. The advantages of this model are (a) no singularity at the wall, and (b) adaptability to separation flows, since R_y instead of y^+ is used as the independent variable in the wall damping function. The model is applicable to more complex flows. The low Reynolds number model is designed to maintain the high Reynolds-number formulation in the log-law region, and is further tuned to fit measurements for the viscous and buffer layers. This approach is adopted in the present work.

As the Mach number of a turbulent flow increases, the velocity fields can no longer be assumed to be solenoidal. Turbulence modeling for compressible flows must be developed to take into account various compressible flow characteristics. To this end, the present study employs a combined model of compressible-dissipation and pressure-dilatation proposed by Sarkar [24-26] along with the low Reynolds number k- ε model. The turbulent kinetic energy and its dissipation rate are calculated from the turbulence transport equations written as follows:

$$\frac{\partial \bar{\rho} k}{\partial t} + \frac{\partial (\bar{\rho} \bar{u}_j k)}{\partial x_j} = \frac{\partial}{\partial x_j} \left(\left(\mu + \frac{\mu_t}{\sigma_k} \right) \frac{\partial k}{\partial x_j} \right) + P_k - \bar{\rho}(\varepsilon_s + \varepsilon_c) + \overline{p'' d''} \quad (13)$$

$$\frac{\partial \bar{\rho} \varepsilon_s}{\partial t} + \frac{\partial (\bar{\rho} \bar{u}_j \varepsilon_s)}{\partial x_j} = \frac{\partial}{\partial x_j} \left(\left(\mu + \frac{\mu_t}{\sigma_\varepsilon} \right) \frac{\partial \varepsilon_s}{\partial x_j} \right) + \frac{(C_{\varepsilon 1} P_k - C_{\varepsilon 2} \bar{\rho} \varepsilon_s)}{T_{\text{turb}}} + A \quad (14)$$

where ε_c and $\overline{p''d''}$ represent compressible-dissipation and pressure-dilatation, respectively, and

$$\varepsilon_c = \alpha_1 M_t^2 \varepsilon_s \quad (15)$$

$$\overline{p''d''} = -\alpha_2 P_k M_t^2 + \alpha_3 \overline{\rho \varepsilon_s} M_t^2 \quad (16)$$

where $M_t^2 = 2k / c^2$ is the turbulent Mach number. The closure coefficients for the compressible corrections are $\alpha_1=1.0$, $\alpha_2=0.4$, $\alpha_3=0.2$

Turbulent quantities of the inflow condition are determined as follows:

$$k = 0.001 u_{inflow}^2, \quad \varepsilon = 0.09 \frac{\rho k^2}{\nu}, \quad \nu = 1.458 e^{-6} \frac{T_{inflow}^{1.5}}{T_{inflow} + 110.4} \quad (17)$$

Turbulent quantities of wall and center line are extrapolated from the interior values.

2.3 Numerical Scheme

The conservation equations for moderate and high Mach-number flows are well coupled, for which standard numerical techniques perform adequately. In regions of low Mach number flows, however, such strong flow coupling breaks down, and the system of conservation equations becomes stiff numerically. Shih and Yang [27] proposed an algorithm based on scaling the pressure terms in the momentum equations and preconditioning the conservation equations to circumvent convergence difficulty at low Mach number. To overcome the numerical stiffness, a dual time-integration procedure designed for all Mach number flows was employed. A second-order time integration was applied to a physical time. The numerical formulation is solved by means of a finite volume approach in which inviscid fluxes are treated by the AUSMPW+[30] and MUSCL(Monotone Upstream-centered Schemes for Conservation Laws) algorithms and viscous fluxes by a central difference algorithm. The code is fully parallelized to speed up the calculation.

The overall numerical approach used for the current research has been validated against several supersonic flow problems [29-31].

3. Result and Discussion

3.1 Physical and Flow Conditions

Figure 1 shows the physical model and the computational domain of concern. The engine designed by a performance analysis code consists of an axisymmetric mixed-compression supersonic inlet, a diffuser, and a combustor with two wedge-type flame holders. The entire engine flow path is considered, extending from the leading edge of the inlet center-body through the exhaust nozzle. The computational domain is divided into eight different zones, consisting of the external zone of two blocks and the internal zone of six blocks. The boundary conditions include the supersonic inflow and outflow, flow symmetry along the centerline, wall boundary, and far-field for the external boundary.

The free stream condition involves a Mach number of 2.1, pressure of 89848.3 Pa, and temperature of 281.8 K. The corresponding flight altitude is 1 km. The fuel used in the present study is Jet-A with an overall equivalence ratio of 1.0. A global reaction mechanism is applied to describe the chemical kinetics. Turbulent combustion is treated using a hybrid kinetic/eddy dissipation model [22]. For simulation of premixed condition, fuel is introduced into the flow path computationally by adding a source term at each cell on the fuel injector plane with a pre specified distribution, mimicking the fuel injection into the air stream from a choked orifice on the wall [19]. Fuel injection plane locates about 0.23 m upstream of the leading edge of flame holders.

3.2 Grid Dependency Test

In order to examine the effects of grid resolution, three grid systems named Level 1, 2, and 3, described in table 1, were considered. The computational domain includes the external flow region and the inlet diffuser, zone 1 through the half of zone 4, where complex flow phenomena like shock-boundary layer interactions and shock train occur, which strongly affect the entire flow quality. The grid points of the zone 1 were adjusted only in zone 1-1 with ramp shocks. Y+ at the 1st ramp region which has the maximum velocity in the

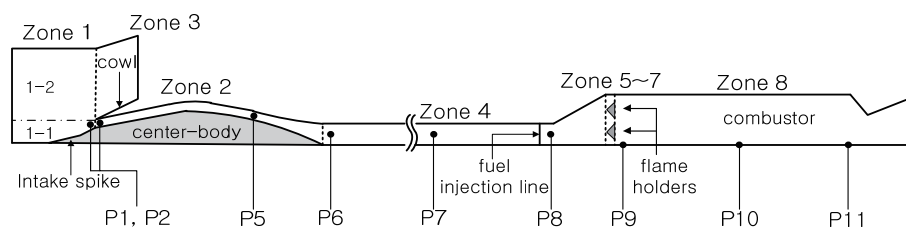


Fig. 1. Physical and computational model with locations of numerical pressure probes

Table 1. Grid system selected for grid dependency test of intake region

	Zone 1-1	Zone 2	Zone 3	The half region of zone 4	Y+	Wall distance, mm
Level 1	84 × 90	190 × 90	81 × 80	50 × 90	≈ 5	5×10^{-3}
Level 2	138 × 120	360 × 120	81 × 80	50 × 120	≈ 5	5×10^{-3}
Level 3	138 × 150	360 × 150	81 × 80	50 × 150	≈ 1	1×10^{-3}

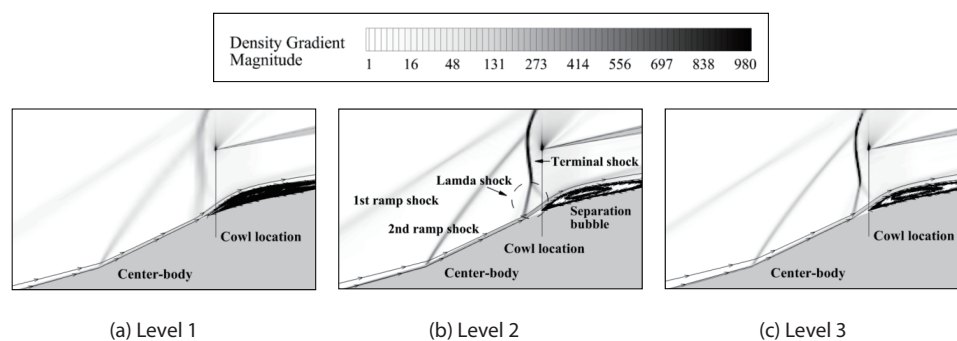


Fig. 2. Density gradient contours near the second ramp of a center body and the inlet cowl

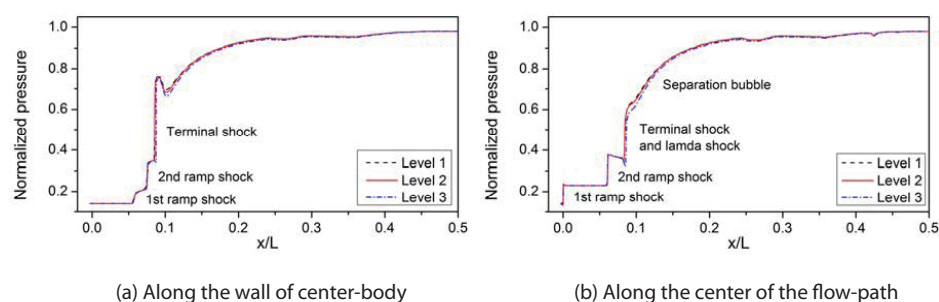


Fig. 3. Normalized pressure along the wall of the center-body and along the center of the flow-path

Table 2. Grid system selected for grid dependency test of combustor region

	The half region of zone 4	Zone 5	Zone 6	Zone 7	Zone 8 without nozzle
Level 1	102 × 90	42 × 31	42 × 31	42 × 30	251 × 150
Level 2	102 × 120	42 × 41	42 × 41	42 × 40	251 × 180
Level 3	102 × 150	42 × 51	42 × 51	42 × 50	251 × 210

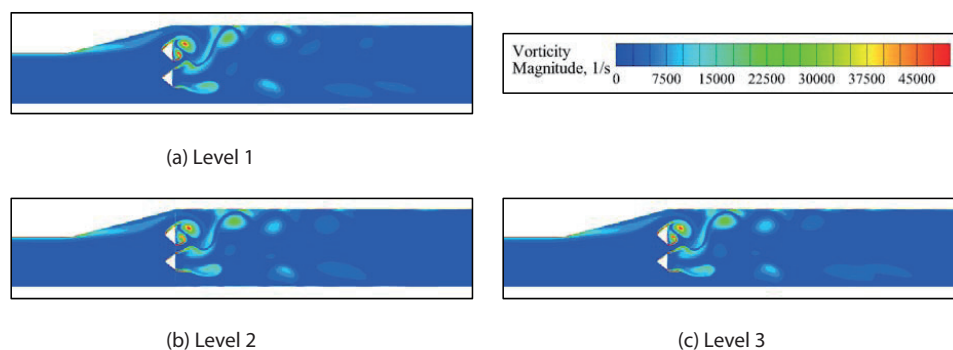


Fig. 4. Vorticity contours near flame holders

engine and the wall distance normal from the solid surface to the first grid point are addressed in Table 1. The free stream conditions include a Mach number of 2.1, pressure of 89848.3 Pa, and temperature of 281.8 K. The outlet boundary condition was set up as subsonic pressure outlet.

Figure 2 and 3 show the detailed flow development near the inlet entrance for each grid system. The normal shock wave stemming from the center body intersects the two oblique shocks originating from the leading cone, and leads to a strong bow shock extending into the external flow region. A small lambda shock wave is presented on the center body surface, due to the interactions between the normal shock wave and boundary layer. In addition, a separation bubble is observed on the surface of the center body. The shock system of Level 1 is thick and indistinct, but Level 2 and 3 represent clear shock structures. So Level 2 grid is applied for this study.

In order to examine the effects of grid resolution in the combustor, three grid systems named Level 1, 2, and 3, described in table 2, were considered. The number of y-direction grid points of each case was identical to that of cases used in zone 4 of intake region. Inlet boundary condition included total pressure of 670 kPa and total temperature of 520 K. The outlet boundary condition was set up as subsonic pressure.

Because combustion characteristic is affected by the vortex shedding near the flame holders, grid system should capture vortex shedding structure. Figure 4 shows vorticity

downstream behind the wedge-type flame holders. The flow structures are quite similar in each grid system. Figure 5 represents vorticity magnitude along $r/R=0.79$ for each grid level and the quite similar shedding behavior of Level 2 and the Level 3. Therefore, the Level 2 grid were applied for efficient computation cost of this study.

3.3 Dominant Pressure Oscillation for Inlet Buzz Operation

The flow conditions were set at a flight Mach number 2.1 at an altitude 1 km. The overall equivalence ratio of the air/fuel mixture is 1.0. In order to simulate the self-sustained inlet buzz, the computational domain includes the entire engine flow path, extending from the leading edge of the inlet center-body through the exhaust nozzle as shown in Fig. 1. Zones 1 and 3 contain 138x199 and 81x80 grid points, respectively, and zone 2 and zones 4 through 8 consist of 360x120, 151x120, 42x41, 42x41, 42x40, and 308x180 grid points, respectively. The grid system of the computational domain from zone1 to the middle of zone 4 is identical to that of Level 2 and then the grid system of other zones was constructed following the grid resolution of Level 2.

Figure 6 shows snapshots of the vorticity, Mach number, temperature, and normalized pressure(based on maximum pressure) fields, zoomed in the inlet and combustor. Air approaches the engine at a Mach number 2.1, passes through a shock train in the compression section at an intake and supersonic diffuser and then mixes with fuel before the flame holder. The Mach number at combustor is very low because of the increase of sonic speed as a temperature increase as chemical reaction takes place in the combustor. A positive value of vorticity corresponds to the counter-clockwise motion. Strong vorticities form along the inlet walls, especially on the cowl side, to satisfy the no-slip condition. The flow separation caused by the shock/boundary-layer interaction, as well as the flow divergence in the downstream region of the center body, also contribute to the generation of vorticity. In addition, vorticity is produced in the combustor due to the flame motion and its interaction with the non-uniform velocity field downstream of the flame holders. Large-scale vorticities are produced and fluctuate at a time scale commensurate with that of the flame fluttering. The frequency contents of flow oscillations at various locations in the engine are examined to provide direct insight into the characteristics and driving mechanisms of unsteady motions.

The pressure oscillations are recorded at locations P1 through P11 to investigate the unsteady motion in the engine (Fig. 7). The overall fluctuations bear strong

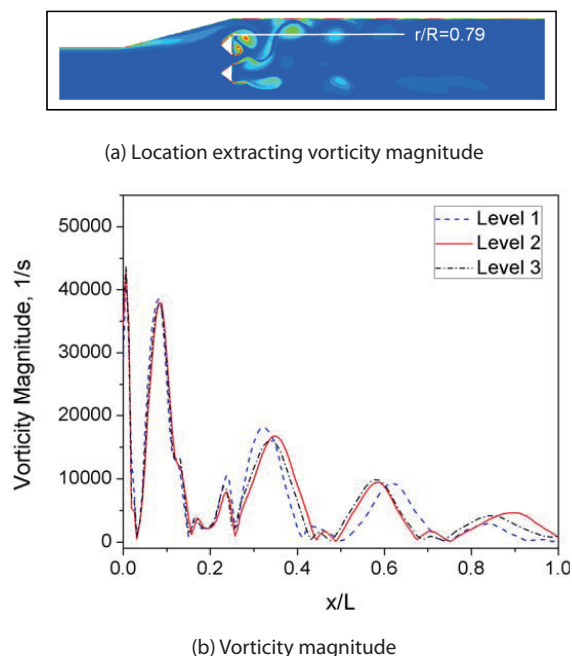


Fig. 5. Location extracting vorticity magnitude and vortex shedding structure along $r/R=0.79$

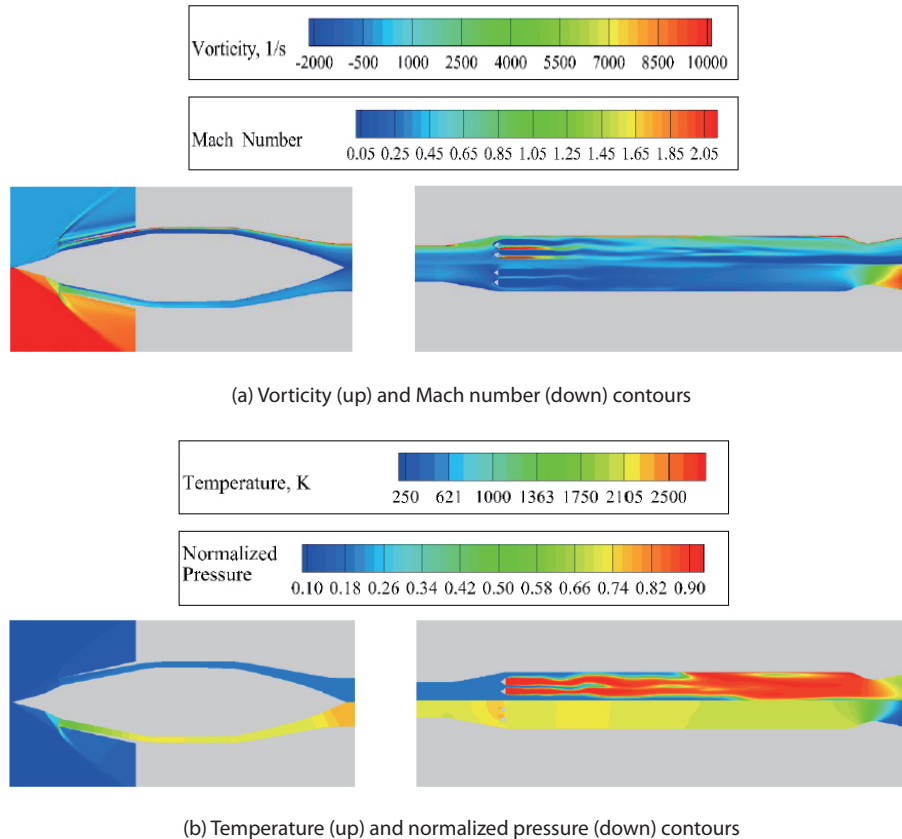


Fig. 6. Snapshots of vorticity, Mach number, temperature, and normalized pressure based on maximum pressure fields zoomed in the inlet and combustor

harmonic oscillation except P1, which is located inside the displacement of the terminal shock train. The bow shock named terminal shock wave oscillates periodically around P1 in response to the acoustic wave produced by the combustion oscillation. The time interval between the peaks of the pressure fluctuation amounts to the oscillation period of the terminal shock train. The pressure amplitude, however, varies according to the shock strength determined by the terminal shock location. The detailed flow structure around of the terminal shock will be discussed later in connection with Figs. 10 and 11. P2 is always located behind the terminal shock. The amplitude of the pressure fluctuation tends to decrease because of the dissipation along the flow path toward the combustor. It abruptly increases at the combustor exit due to the vortex-induced acoustic oscillation in the contraction region of the nozzle. Figure 8(b) shows the frequency spectra of pressure signals. The dominant frequencies of pressure fluctuations have the values of 294 Hz and 600 Hz at all the locations, except for P1 which exhibits a broad distribution. The dominant pressure oscillation may mainly related with the buzz motion of terminal shock because it changes not only acoustic

wave's boundary condition, but the amount of air mass flow delivered into the intake as the terminal shock wave locates outside and inside of the cowl tip. Figure 8 shows the temporal evolution of the inlet air mass flow delivered into the engine and its frequency contents. The variation of the air mass flow rate is about 5% of average value. The major frequency is around 294 Hz, identical to the situation with the pressure oscillations. The phases, however, are different, as evidenced in Fig. 9. The terminal shock moves back and forth in the inlet, thereby producing oscillations of the inlet air supply in accordance with the combustion oscillation frequency of 294 Hz [12, 18].

3.4 Terminal Shock Train for Inlet Buzz Operation

Figures 9 and 10 show the temporal evolution of the flow dynamics near the cowl lip within a buzz cycle. The figures from (a) through (h) in Fig. 9 and Fig. 10 are in accord with the temporal points from "a" through "h" represented in Fig. 11. The cycle starts at point 'a' in Fig. 11. As the terminal shock moves upward, the pressure magnitude at P2 decreases (see "NP of 0.68 and 0.755" moving downstream) as shown in Fig.

9 (a) through Fig. 10 (d) because the pressure wave evacuates through the gap between the terminal shock and the cowl lip, after “NP=0.755” moves upstream, and the pressure

builds up. The terminal shock is first disgorged out of the cowl lip, then moves downstream, and finally stays at the cowl lip. Such a process of the terminal shock motion occurs

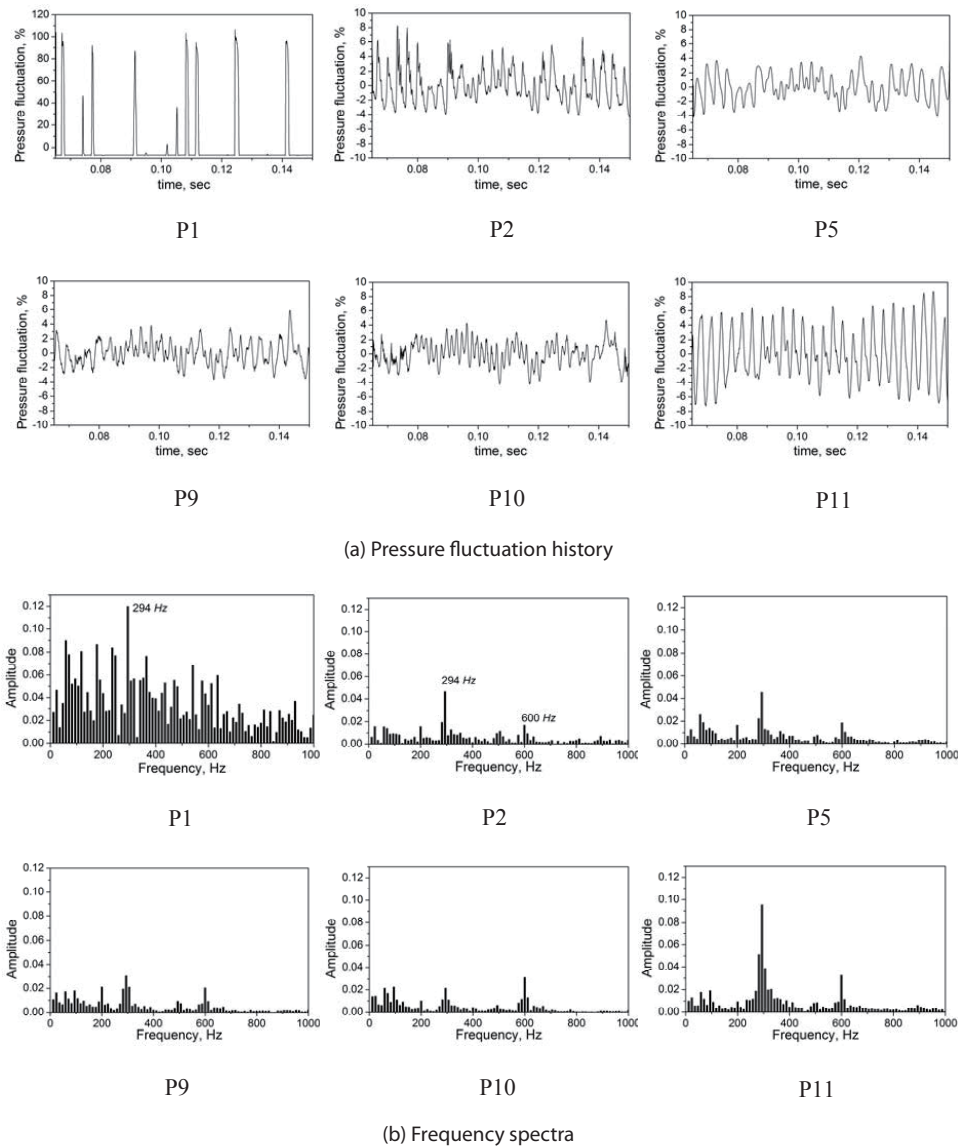


Fig. 7. Pressure fluctuation and frequency spectra recorded at P1, P2, P5, P9, P10, and P11

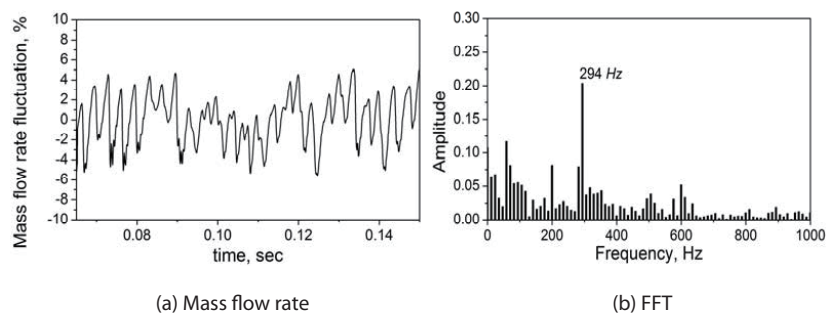


Fig. 8. History and frequency spectra of mass flow rate fluctuation recorded at the inlet

periodically. Figures 9(i) and 10(i) show that the moving distance of pressure waves, $NP=0.68$ and 0.755 , and terminal shock for one buzz cycle. The oscillation period may be determined by the complex coupling between the inlet and combustor flow dynamics which discussed in paragraph 3.5.

Figure 10 shows the contours of the density gradient magnitude. The shock structures and their interactions with the boundary layers are clearly observed. Strong vorticity is produced by the shock/boundary layers interactions and the flow divergence in the downstream region of the center body. The geometric variation of the recirculating region is dictated by the relative strength of the two vorticity-production mechanisms. The location of the shock-induced boundary-layer separation and associated flow structure specially separation bubble play an important role determining the terminal shock train. The separation bubble increases boundary layer thickness and reduces the cross section area of flow-through so that it prohibits the terminal shock moving further downstream which can be supported

by the Fig. 10(i).

3.5 Interactions between Inlet Buzz and Combustion Oscillation

As shown in Figs. 7 and 8, pressure oscillations with well-defined frequencies prevail in the entire flow path of the engine. The terminal shock movements back and forth during inlet buzz results in the change of both the air mass flow rate delivered into the inlet and total pressure of inlet air so it is valuable to investigate the dynamic behavior of mass flow fluctuation and pressure oscillation in the engine. The air mass flow rate and the pressure fluctuation for a buzz operation have different fluctuation history as shown in Fig. 11. While mass flow rate decreases as the terminal shock moves further away from the inlet cowl because increased spillage of incoming air mass, the pressure behind the terminal shock, P_2 increases oppositely due to strong bow shock. The opposite trend can be expected as the terminal

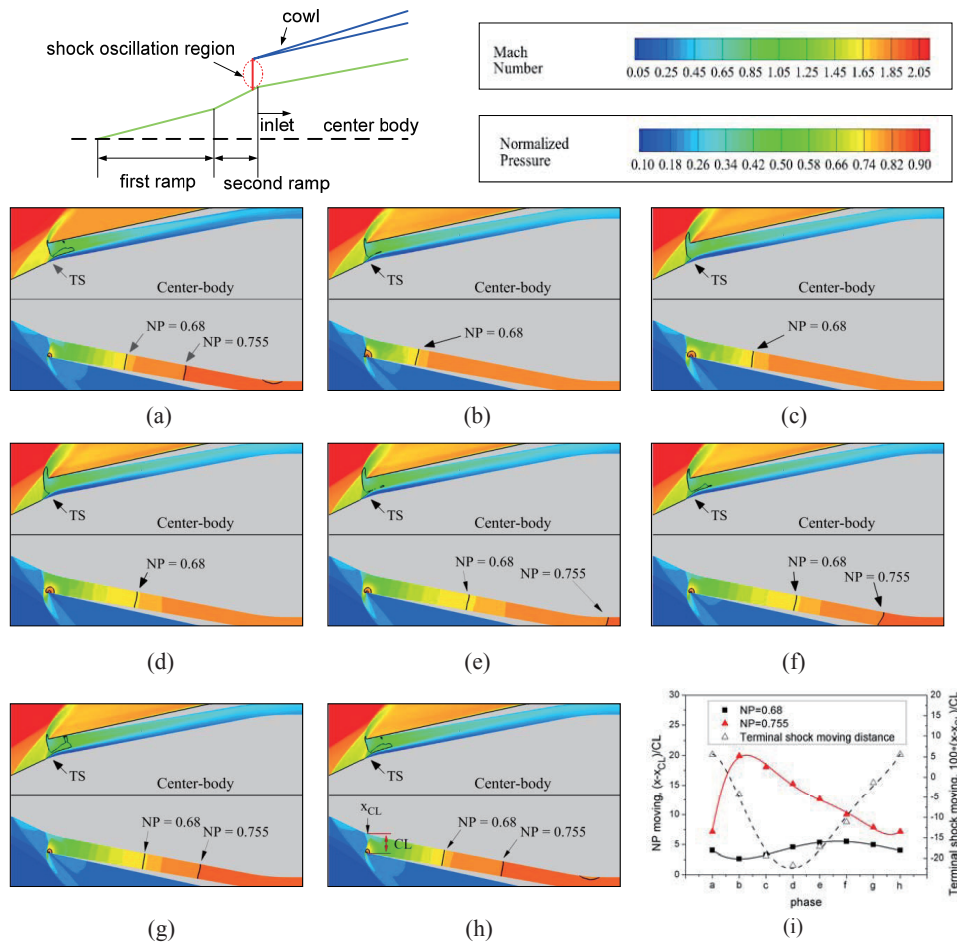


Fig. 9. Detail inlet flow structure during one buzz cycle: 1) terminal shock (TS) oscillation (up) described by Mach flood contour and Mach number line of 1.0, and 2) pressure wave (down) described by normalized pressure (NP based on the maximum pressure value in whole simulation) flood and line contour and 3) (i) moving distance of two pressure waves and the terminal shock from the cowl tip.

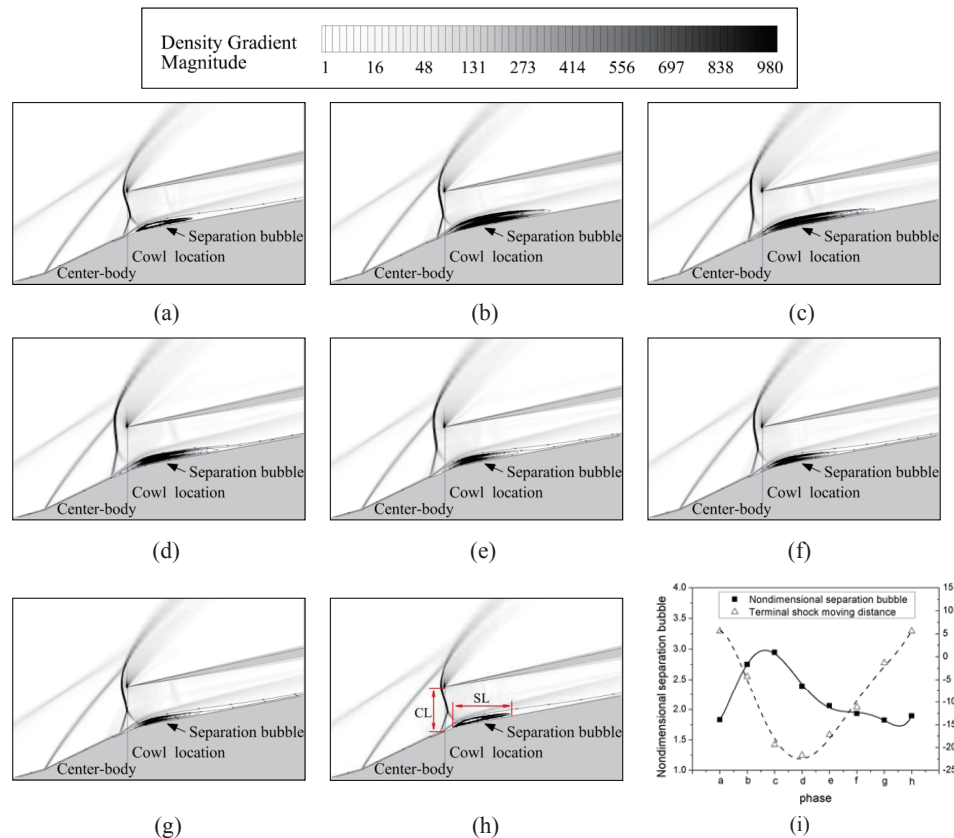


Fig. 10. Density gradient magnitude contours near the second ramp of a center body and the inlet cowl during one buzz cycle : The terminal shock moving distance from the cowl-location is based on CL and non-dimensional separation bubble size is the ratio of SL to CL

shock approaches to the inlet cowl. The pressure change behind the terminal shock influences the pressure in the entire flow path of the engine. Both pressure immediately downstream of the terminal shock (P2) and pressure at the center of the combustor (P10) fluctuate at the same frequency of 294 Hz, but with out of phase.

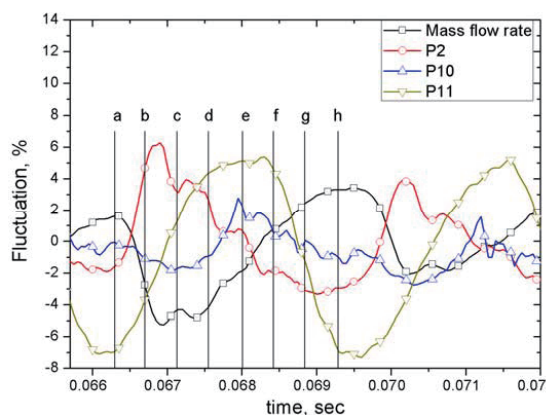


Fig. 11. Fluctuation history of mass flow rate at the inlet and pressure at P2, P10, and P11

Figure 12 presents snapshot of temperature contours and the fuel mass fraction in the combustor within a buzz cycle with $f=294$ Hz. Flames are highly oscillatory because the vortical motion behind the flame holders influences the fuel-air mixing. As a result, the oscillatory flames anchored at the flame holders aggravate the pressure and temperature fluctuations, which subsequently wrinkle the flame fronts through the influence of the complex vortical field. Unburnt gases along the combustor wall and in the center region affect the local heat release rate and ensuing pressure and vorticity fluctuations, thereby causing variations of the oscillation frequencies. The combustion completes in the rear region of the combustor.

4. Conclusions

A unified numerical analysis was conducted to study the inlet buzz and combustion oscillation in an axisymmetric ramjet engine which consists of a mixed-compression supersonic inlet and two wedge-hollow-cone-type flame

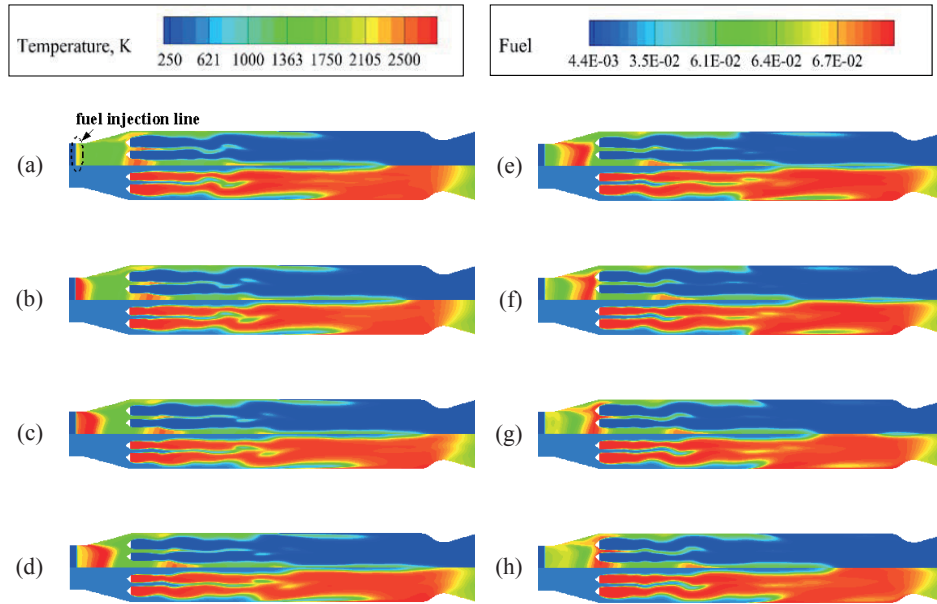


Fig. 12. Snapshots of fuel mass-fraction(up) and temperature(down) contours in the combustor within a buzz cycle

holders. The physical domain of concern includes the entire engine flow path, extending from the leading edge of the inlet center-body through the exhaust nozzle. Major results from the present study are summarized as follows;

1) As a consequence of the oscillatory motion of the terminal shock around the inlet cowl lip, i.e. inlet buzz, the rate of the air mass flow delivered into the combustor varies.

2) The flow separation as well as a volumetric expansion or contraction of the flow recirculation occurs according to the strength of shock/boundary interaction. The location of the shock-induced boundary-layer separation and separation bubble structure play an important role determining the buzz characteristics.

3) Both pressure immediately downstream of the terminal shock (P2) and pressure at the center of the combustor (P10) fluctuate at the same frequency of 294 Hz, but with out of phase.

4) The terminal shock outside of the cowl decreases the inlet air mass delivered into the intake because of air spillage. And the chamber pressure decreases due to the decreased total mass flow rate of air and fuel at a typical fuel-air ratio. And then the terminal shock moves downstream to the inlet cowl because the decreased pressure behind terminal shock induced by the decreased chamber pressure. However the terminal shock can move downstream only to a typical location where a recirculation bubble occurs. And then the chamber pressure increases again because the amount of air delivered into the intake increases as the terminal shock

locates inside of intake, i.e. no or small air spillage. And then the increased chamber pressure pushes the terminal shock outside of the cowl again. So the inlet buzz operates.

References

- [1] K. Oswaititsch, *Pressure Recovery for Missiles with Reaction Propulsion at High Supersonic Speeds*, NACA TM-1140, Jun. 1947.
- [2] A. Ferri, and R.M. Nucci, *The Origin of Aerodynamic Instability of Supersonic Inlets at Subcritical Conditions*, NACA RM-L50K30, Jan. 1951.
- [3] C. L. Daily, "Supersonic Diffuser Instability," *Journal of the Aeronautical Sciences*, Vol. 22, No. 11, Nov. 1955, pp. 733-749.
- [4] T. Nagashima, T. Obokato, and T. Asanuma, *Experiment of Supersonic Air Intake Buzz*, Institute of Space and Aeronautical Science, University of Tokyo, Japan, Rept. 481, May 1972.
- [5] H. Mirels, *Acoustic Analysis of Ram-Jet Buzz*, NACA TM, NO. 3574-1140, 1955
- [6] R. L. Trimpi, *A Theory for Stability and Buzz Pulsation Amplitude in Ram Jets and an Experimental Investigation Scale Effects*, NACA Rept. 1256, 1953
- [7] J. T. Slimon, T. J. Bogar, and M., Sajben, "Laser Doppler Velocimeter Measurements in Unsteady, Separated, Transonic Diffuser Flows," *AIAA Journal*, Vol. 21, Dec. 1983,

pp. 1690- 1697

[8] M. Sajben, T. J. Bogar, and J. C. Kroutil, "Forced Oscillation Experiments in Supercritical Diffuser Flows," *AIAA Journal*, Vol. 22, Apr. 1984, pp. 465- 474.

[9] T. J. Bogar, M. Sajben, and J. C. Kroutil, "Response of Supersonic Inlet to Downstream Perturbations," *Journal of Propulsion and Power*, Vol. 1, Mar.-Apr. 1985, pp. 118-125.

[10] J. G. Bemdot, A. E. Heins, and T. G. Piercy, *Ramjet Air Induction System For Tactical Missile Application*, AGARD-LS-136, 1984, pp. 2.1-49.

[11] T. Hsieh, T. J. Bogar, and T. J. Coakley, "Numerical Simulation and Comparison with Experiment for Self-Excited Oscillations in a Diffuser Flow," *AIAA Journal*, Vol. 25 No. 7, 1987, pp. 936-943.

[12] V. Yang, and F. E. C. Culick, "Analysis of Unsteady Inviscid Diffuser Flow with Shock Wave," *Journal of Propulsion and Power*, Vol. 1, 1985, pp. 222-228.

[13] V. Yang, and F. E. C. Culick, "Analysis of Low Frequency Combustion Instabilities in a Laboratory Dump Combustor," *Combustion Science and Technology*, Vol. 45, 1986, pp. 1-25.

[14] J. E. Crump, K. C. Schadow, F. E. C. Culick, and V. Yang, "Longitudinal Combustion Instabilities in Ramjet Engines: Identification of Acoustic Modes," *Journal of Propulsion and Power*, Vol. 2, 1986, pp. 105-109.

[15] R. W. Newsome, "Numerical Simulation of Near-Critical and Unsteady, Subcritical Inlet Flow," *AIAA Journal*, Vol. 22, No. 10, 1984, pp. 1375-1379.

[16] P. J. Lu, and L. T. Jain, "Numerical Investigation of Inlet Buzz Flow," *Journal of Propulsion and Power*, Vol. 14, No. 1, 1998, pp. 90-100.

[17] J. Y. Oh, F. H. Ma, S. Y. Hsieh, and V. Yang, "Interactions between Shock and Acoustic Waves in a Supersonic Inlet Diffuser," *Journal of Propulsion and Power*, Vol. 21, 2005, pp. 486-495.

[18] S. Y. Hsieh and V. Yang, "A Unified analysis of Unsteady Flow Structures in a Supersonic Ramjet Engine," *Proceedings of International Colloquium on Advanced Computation and Analysis of Combustion*, Moscow, Russia, 1998.

[19] H.-G. Sung and V. Yang, "Unified Analysis of Internal Flowfield in an Integrated Rocket Ramjet Engine, I: Transition from Rocket Booster to Ramjet Sustainer," *Journal of Aerospace Engineering*, Vol. 27, No. 2, 2014, pp. 390-397.

[20] H.-G. Sung and V. Yang, "Unified Analysis of Internal Flowfield in an Integrated Rocket Ramjet Engine, II: Ramjet

Sustainer," *Journal of Aerospace Engineering*, Vol. 27, No. 2, 2014, pp. 398-403.

[21] J. Lee, and D. Fricker, "A Numerical Study of Reacting Flow inside Combustors using a Two-equation model of Turbulence and an Eddy-dissipation Model of Turbulent Chemistry," *Aerospace Sciences Meeting and Exhibit*, 35th, Reno, NV, Jan. 6-9, 1997.

[22] B. F. Magnussen, and B. H. Hjertager, "On Mathematical Modeling of Turbulent Combustion with Special Emphasis on Soot Formulation and Combustion," *16th Int'l Symposium on Combustion*, The Combustion Institute, 1976, pp. 719-729.

[23] Z. Yang, and T. H., Shih, "New Time Scale Based Model for Near-Wall Turbulence," *AIAA Journal*, Vol. 31, No. 7, 1993, pp. 1191- 1197.

[24] S. Sarkar, B. Erlebacher, M. Hussaini, and H. Kreiss, "The Analysis and Modeling of Dilatational Terms in Compressible Turbulence," *Journal of Fluid Mechanics*, Vol. 227, 1991, pp. 473-493.

[25] S. Sarkar, "Modeling the Pressure-Dilatation Correlation," *ICASE*, Rept. 91-42, May 1991

[26] S. Dash, and D. C. Kenzakowski, "A Compressible-Dissipation Extension of the k-Epsilon Turbulence Model and Building-Block Data for its Validation," *AIAA and SDIO*, Annual Interceptor Technology Conference, Huntsville, AL, May 19-21, 1992

[27] D. C. Wilcox, *Effects of Compressibility*, Chap. 5 of Turbulence Modeling for CFD, 2nd Ed., DCW Industries Inc., 1998

[28] K. H. Kim, C. A. Kim, and O. H. Rho, "Methods for the Accurate Computations of Hypersonic Flows," *Journal of Computational Physics*, Vol. 174, No. 1, 2001, pp. 38-80.

[29] H.-G. Sung, H. W. Yeom, S. Yoon, and, J. Kim, "Investigation of Rocket Exhaust Diffusers for Altitude Simulation," *Journal of Propulsion and Power*, Vol. 26, No. 2, pp. 240-247, 2010.

[30] H. W. Yeom, S. Yoon, and H. G. Sung, "Flow Dynamics at the Minimum Starting Condition of a Supersonic Diffuser to Simulate a Rocket's High Altitude Performance on the Ground," *Journal of Mechanical Science and Technology*, Vol. 23, No. 1, 2009, pp. 254-261.

[31] J. Y. Heo, and H. G. Sung, "Fluidics Thrust Vector Control of Supersonic Jet Using Co-flow Injection," *Journal of Propulsion and Power*, Vol. 28, No. 4, 2012, pp. 858-861.